PCCP

PAPER

View Article Online
View Journal | View Issue

Cite this: *Phys. Chem. Chem. Phys.*, 2019, **21**, 2572

A novel hydrogenated boron–carbon monolayer with high stability and promising carrier mobility†

Dong Fan, ‡ Shaohua Lu,‡ Chengke Chen, Meiyan Jiang, Xiao Li and Xiaojun Hu *

Received 11th October 2018,
Accepted 14th December 2018

DOI: 10.1039/c8cp06346j

rsc.li/pccp

Although immense research on the extension of the two-dimensional (2D) material family has been carried out, 2D materials with a satisfactory band gap, high carrier mobility, and outstanding thermodynamic stability under ambient conditions are still limited. In this work, using first principles calculations, we proposed new 2D ternary materials consisting of C, B, and H atoms, namely hexagonal-BCH (h-BCH) and tetragonal-BCH (t-BCH). Both phonon calculations and *ab initio* molecular dynamics simulations show that these proposed sheets are thermodynamically stable phases. The electronic structure calculations indicate that h-BCH and t-BCH sheets are semiconductors with a band gap of 2.66 and 2.22 eV, respectively. Remarkably, the h-BCH (t-BCH) sheet exhibits electron mobility as high as 7.41×10^3 (1.09×10^3) $cm^2\ V^{-1}\ s^{-1}$, which is higher than that of the MoS_2 monolayer, though the hole mobility is about one (two) order of magnitude lower. Equally important is the fact that the position of both the conduction and valence band edges of the h-BCH sheet matches well with the chemical reaction potential of H_2/H^+ and O_2/H_2O, giving a 2D photocatalyst as a potential candidate for overall visible-light-driven water splitting. Therefore, the designed h-BCH and t-BCH monolayers have promising applications in future electronics and photocatalysts.

1 Introduction

Two-dimensional (2D) crystals have received significant attention in recent years, because of their potential applications in catalysis, electronics, electrochemical energy storage, and spintronic devices.[1–5] As compared to their bulk counterparts, the physical and chemical properties of 2D materials can be easily tailored by adapting external strain, controlling defects, or stacking multiple layers of 2D structures by van der Waals interactions.[6–8] All these advantages endow 2D materials with potential for applications in catalysis, sensors, photocatalysis, and nanophotonics.[1–8] Graphene is famous for its superior physical properties including excellent mechanical strength, high electrical conductivity, and transporting properties. However, an intrinsic zero-band-gap of pristine graphene is disadvantageous for application in electronic devices;[9,10] few-layer black phosphorus with high carrier mobility (up to $\sim$1000 $cm^2\ V^{-1}\ s^{-1}$) is another alternative material, while its instability in air will lead to speedy performance deterioration.[11,12] Thus, although immense research on the extension of the 2D material family has been carried out, 2D materials with a satisfactory band gap, high carrier mobility, and outstanding thermodynamic stability under ambient conditions are still limited.

It was widely reported that controlled functionalized modifications, including oxidation and hydrogenation, were powerful techniques to tune the chemical properties of 2D crystals. A wide range of graphene derivatives with tunable chemical properties was demonstrated.[13–15] Apart from graphene, four stable hydrogenated borophene sheets with massless Dirac fermions and high stability were reported;[16] the tunable electronic and optical properties of oxidized blue phosphorene (or blue phosphorene oxide) were investigated.[17] Recently, Pan *et al.* designed an organic C_4N_3H monolayer with high Fermi velocity, inspired by the experimentally synthesized C_2N-h2D structure;[18,19] a single-layer borophene hydride sheet with high thermal conductivity and attractive optical properties was reported by Mortazavi *et al.*[20] These results suggested that 2D materials with improved performance had been realized by using oxidation or hydrogenation technology.

Herein, motivated by our previous work on 2D B–C and Si–C binary sheets,[21,22] and by the experimentally accessible hydrogenation process, we propose two hitherto-unknown 2D materials that we term as h-BCH and t-BCH because their structures can

College of Materials Science and Engineering, Zhejiang University of Technology, Hangzhou 310014, China. E-mail: huxj@zjut.edu.cn; Fax: +86-571-88871522; Tel: +86-571-88871522

† Electronic supplementary information (ESI) available: Calculated lattice parameters, elastic constants, and in-plane Young's modulus of t-BCH and h-BCH sheets. The structural data in this work, and the output of *NVT*-MD simulation results, which support the findings of this study, are available at https://github.com/agrh/Papers. See DOI: 10.1039/c8cp06346j

‡ These authors contributed equally to this work.

be viewed as hexagonal and tetragonal lattices, respectively. According to our phonon dispersion calculations, mechanical parameter calculations, and *ab initio* molecular dynamics (AIMD) simulations, we demonstrate that h-BCH and t-BCH sheets are dynamically, mechanically, and thermally stable. h-BCH (t-BCH) is predicted to be a semiconductor with a band gap of 2.66 (2.22) eV and a high carrier mobility of 7.41 (1.09) $\times$ 10^3 cm^2 V^{-1} s^{-1}, dramatically higher than that of semiconducting H–MoS_2 ($\sim$200 cm^2 V^{-1} s^{-1}),[23] rendering the h-BCH (t-BCH) monolayer a promising 2D material for electronic applications. Of particular importance is the fact that the calculated band edge positions indicate that h-BCH is a promising candidate as an efficient photocatalyst for overall water splitting.

2 Computational methods

All calculations were performed in the Vienna *ab initio* Simulation Package (VASP) based on density functional theory (DFT) and the projector augmented wave (PAW) method.[24,25] A basis of plane waves with an energy cutoff of 650 eV was used to expand the valence electron wave functions. The electronic exchange–correlation interaction was treated by using the Perdew–Burke–Ernzerhof (PBE) functional within the generalized gradient approximation (GGA).[26] The Heyd–Scuseria–Ernzerhof (HSE06) functional was adopted to calculate the accurate band structure.[27] A slab model containing a 15 Å vacuum region was chosen to simulate the isolated 2D crystals. Geometry optimization was carried out by using convergence criteria of 10^{-5} eV for energy and 10^{-2} eV per Å for force. The first Brillouin zone was set with a 20 $\times$ 20 $\times$ 1 and 12 $\times$ 12 $\times$ 1 Monkhorst–Pack special *k*-point mesh for h-BCH and t-BCH, respectively. For the calculation of mobility, a dense *k*-point mesh along the Brillouin zone directions was used, *i.e.*, 100 spaced *k*-points were used along the *Γ*–*X* direction in the Brillouin zone of the t-BCH monolayer. Phonon calculations were performed by using the Phonopy code.[28] Thermal stability is also investigated by using AIMD simulations with a time step of 1 fs for a total time of 5 ps. The DFT-D2 method with the van der Waals force correction was also chosen to describe the possible long-range interactions.[29] The strain is defined as $\varepsilon = (a - a_0)/a_0$, where a and a_0 are the lattice constants with and without strain, respectively.

3 Results and discussion

3.1 Geometric structures

The design of h-BCH and t-BCH was inspired by our previously proposed B_4C_3 sheet containing a novel hexa-coordinated sp^2 carbon moiety and a t-SiC sheet containing a quasi-planar four-coordinated carbon moiety, respectively.[21,22] Fig. 1a presents the top and side views of the atomic structure of h-BCH with the *P*3*m*1 space group. This structure is described by a hexagonal primitive cell. The optimized lattice constants are $a = b = 2.62$ Å, featured by one C atom surrounded by six B–C bonds. The length of the C–B bond (1.72 Å) in h-BCH monolayer is slightly shorter than that in the B_4C_3 sheet ($\sim$1.77 Å).[21]

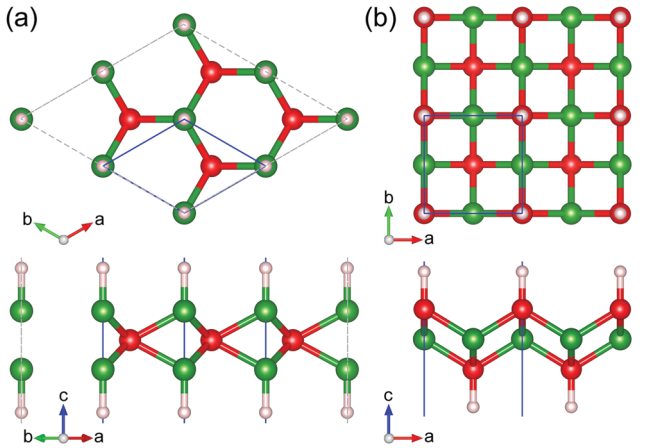

Fig. 1 Top (upper) and side (lower) views of the optimized structure of (a) h-BCH and (b) t-BCH monolayers. The blue lines denote the unit cell. The red, green, and white balls represent carbon, boron, and hydrogen atoms, respectively.

Simultaneously, the length of the B–H bond is consistent with that of the previously proposed 2D boron–hydride sheets (1.19 Å).[16] However, in the t-BCH monolayer, the hydrogen atoms are located on both sides of tetragonal B–C planes forming a puckered structure, which belongs to the *P*4/*nmm* space group. The C–B and C–H bond lengths are calculated to be 1.67 and 1.09 Å, respectively.

3.2 Stabilities

First, to assess the energetic stability of the proposed monolayers, we calculated the cohesive energy (E_{coh}), as defined by $E_{coh} = (n_C E_C + n_B E_B + n_H E_H - E_B CH)/(n_C + n_B + n_H)$, where E_C, E_B, E_H, and E_{BCH} are the calculated total energies of isolated C, B, and H atoms and the corresponding BCH monolayer, respectively; n_C, n_B, and n_H are the number of C, B, and H atoms in the unit cell of the monolayer, respectively. According to our computations, the cohesive energy of the proposed sheets determined from the difference in the total energy between the h-BCH (t-BCH) sheet and isolated B, C, and H atoms is 5.53 (4.90) eV per atom, indicating that the monolayers can be stable. As a reference, the cohesive energies of silicene and phosphorene, which have been synthesized experimentally,[3,30] were reported to be 3.71 and 3.61 eV per atom, respectively.[31] Therefore, the even higher cohesive energy ensures that t-BCH and h-BCH are strongly bonded networks.

Next, the dynamic stability is further determined by the phonon dispersion calculations, which show no imaginary frequency in the whole Brillouin zone, as shown in Fig. 2. This means that t-BCH and h-BCH are dynamically stable and possess local energy minima. As expected, the detailed analysis of partial phonon density of states (Ph DOS) reveals that the highest frequency of h-BCH and t-BCH monolayers is mainly contributed by B–H and C–H bonds, respectively. Moreover, AIMD simulations demonstrate that these monolayers are also stable under ambient conditions. We consider the 4 $\times$ 4 supercell of h-BCH containing 80 atoms, and the 3 $\times$ 3 supercell of the t-BCH

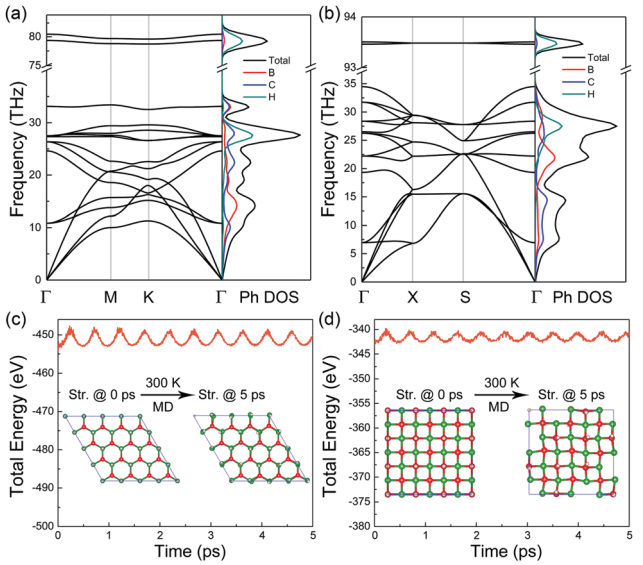

Fig. 2 Phonon dispersion curves of (a) h-BCH and (b) t-BCH. Evolution of the total energy and snapshots of (c) h-BCH and (d) t-BCH from AIMD simulations at 0 and 5 ps.

monolayer containing 54 atoms. The simulations lasted for 5.0 ps with a time step of 1.0 fs. As shown in Fig. 2, h-BCH and t-BCH can maintain their monolayer structures after AIMD simulations at 300 K for 5.0 ps. The evolution of the total energy and snapshots of h(t)-BCH after AIMD simulations at 500 and 700 K are shown in Fig. S1 (ESI†). Clearly, for the h-BCH monolayer, significant atomic rearrangement took place and was substantially disordered after AIMD simulations at 500 and 700 K. However, from the snapshots, the t-BCH monolayer was found to maintain its structural integrity even at 700 K. Hence, h-BCH can maintain its structural integrity at room temperature while t-BCH remains stable even at 700 K, revealing that both of the proposed monolayers show satisfactory dynamic stabilities. It is also essential to consider their structural stability in the aqueous environment using AIMD simulations.[32] Further analysis of the AIMD simulations with the interaction of water molecules also reveals the high stability of the structures at 300 K, as shown in Fig. S2 (ESI†) (with low density of H_2O molecules) and Fig. S3 (ESI†) (with high density of H_2O molecules). Clearly, all proposed sheets can maintain their structural integrities either with or without the existence of water molecules at room temperature.

Additionally, we verify the mechanical stabilities of h-BCH and t-BCH by estimating their elastic constants. In general, for a mechanically stable 2D structure, the calculated elastic constants should satisfy $C_{11}C_{22} - C_{12}C_{21} > 0$ and $C_{66} > 0$.[33] For h-BCH, we used a rectangular lattice to calculate its elastic constants, and all the calculated results are listed in Table S1 (ESI†). All elastic constants of the structures satisfy the above-mentioned criteria, suggesting that h-BCH and t-BCH sheets have favorable mechanical stabilities. The in-plane stiffness is $E = (C_{11}^2 - C_{12}^2)/C_{11}$ = 223 N m^{-1} for h-BCH (233 N m^{-1} for t-BCH), which is lower than that of graphene (340 N m^{-1}),[34] but higher than or comparable to that of the C_4N_3H monolayer (173.1 and 114.3 N m^{-1}),[18] t-SiC (105 and 119 N m^{-1}),[22] MoS_2 (140 N m^{-1}),[35] tetr-TiC (202 N m^{-1}),[36] and TiNX (X = F, Cl, Br, 181–229 N m^{-1}).[4] The high in-plane stiffness also essentially reflects the robust bonding feature of h-BCH and t-BCH.

3.3 Electronic structures and carrier mobilities

We then investigate the electronic properties of these new sheets using the hybrid functional (HSE06), due to the well-known significant underestimation of the band gaps of the conventional DFT calculation. The calculated band structures of h-BCH and t-BCH are shown in Fig. 3a, revealing that h-BCH shows an indirect band gap (2.66 eV), in contrast, t-BCH possesses a direct band gap of 2.22 eV. For h-BCH, its conduction band minimum (CBM) is located at the *k*-point, while the valence band maximum (VBM) is located at the *Γ*-point. However, the VBM and the CBM of t-BCH are both located at the *Γ*-point. The partial densities of states (DOS) of the sheets, shown in Fig. S4 (ESI†), indicate that the main contribution to the valence band and conduction band stems from B-p and C-p states (also see Fig. 3b), while the contribution of s-states of the H atom is negligible. However, the H-s orbital is mainly distributed in the energy range of 0.5–1.5 eV in h-BCH and 3–5 eV in t-BCH below the VBM, indicating a strong hybridization between boron and hydrogen atoms and a covalent bonding feature with both B and C atoms. To further elucidate the

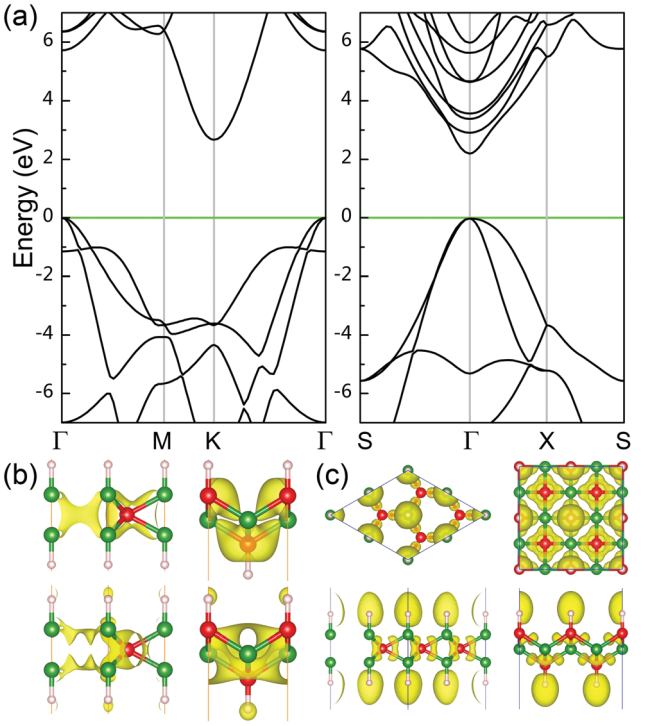

Fig. 3 (a) Calculated HSE06 band structures of h-BCH (left) and t-BCH (right). The Fermi level (green line) is set to zero. (b) The highest occupied orbital (upper) and the lowest unoccupied orbital (lower) at the high symmetry point for h-BCH (left) and t-BCH (right), respectively. The isosurface value is set to 0.001 e per Å^3. (c) Top (upper) and side (lower) views of the electron localization function (ELF) for h-BCH (left) and t-BCH (right), respectively. The isovalue is set to 0.75.

bonding nature of the proposed structure, we then calculated the electron localization function (ELF) to analyze its electron distributions, as shown in Fig. 3c. It can be seen that the ELF patterns are clearly located between the C–B and C–H bonds, suggesting that these bonds have robust covalent electron states with σ-like sp^2-hybridization for h-BCH.[21]

From the calculated electronic band structure of the proposed structures, it can be clearly seen that the conduction bands are dispersive significantly, suggesting a potential high electron mobility. To confirm this conjecture, we calculated the carrier mobilities of h-BCH and t-BCH, on the basis of the obtained effective mass (m^*), deformation potential constants (E_1), and 2D elastic modulus (C_{2D}). The carrier mobility is given by the expression:[37–39]

$$\mu = \frac{e\hbar^3 C_{2D}}{k_B T m_e^* m_d (E_l^i)^2} \quad (1)$$

where $\hbar$ is the reduced Planck's constant, e is the electron charge, m_e^* is the effective mass along the transport direction; m_d is the average effective mass determined by $m_d = \sqrt{m_x^* m_y^*}$; and the term E_l denotes the deformation potential constant of the CBM for electrons and the VBM for holes along the transport direction, described by equation: $E_l^i = \Delta V_i/(\Delta l/l_0)$, where ΔV_i is the energy change of the ith band under moderate compression and tension (using a step of 0.5%, see Fig. S5 and S6, ESI†); l_0 is the lattice constant along the transport direction; and Δl is the deformation of l_0. The elastic modulus C_{2D} is derived using equation: $C_{2D} = h([C_{11}^2 - C_{12}^2]/C_{11})$, where C_{11} and C_{12} represent elastic constants (GPa) given by VASP and h represents the height of the cell (Å) for structures.[33,38,40]

The calculated m^*, E_l, C_{2D}, and mobility values are summarized in Table 1. One can see that the calculated m^* values of electrons are smaller than those of the holes, owing to the flat valence band and a more dispersive conduction band of the structures. The flat valence band feature also results in extremely low hole mobility in both directions. The highest electron mobility for h-BCH is predicted to be 7.41×10^3 cm^2 V^{-1} s^{-1} at 300 K, which is significantly higher than that of the previously reported MoS_2 monolayer (~200 cm^2 V^{-1} s^{-1}),[23] and comparable with that of black phosphorus (~1.13×10^3 cm^2 V^{-1} s^{-1}),[38] suggesting its promising application potential for future nano-electronics. For t-BCH, the electron mobility is 1.04×10^3 cm^2 V^{-1} s^{-1}, (along the Γ–X direction) while the hole mobility is 44 cm^2 V^{-1} s^{-1}. Therefore, for these two structures, the electron mobilities could be comparable to or even higher than that of many previously proposed 2D semiconductors, such as Group 15 monolayers,[1] single-layer Tl_2O,[41] and Te-based monolayers.[42]

Table 1 Calculated effective mass (m^*, [m_0]), deformation potential constant (E_l, [eV]), 2D elastic modulus (C_{2D}, [N m^{-1}]), and mobility (μ_{2D}, [$\times 10^3$ cm^2 V^{-1} s^{-1}]) for electrons and holes along different directions at 300 K

	Carrier type	m^*	E_l	C_{2D}	μ_{2D}
h-BCH	Electron (Γ–Y)	0.332	2.43	222.7	7.32
	Electron (Y–Γ)	0.328	2.43	222.7	7.41
	Hole (Γ–Y)	0.541	6.96	222.7	0.327
	Hole (Γ–X)	0.564	6.82	222.7	0.326
t-BCH	Electron (Γ–Y)	0.310	6.84	232.6	1.09
	Electron (Γ–X)	0.314	6.98	232.4	1.04
	Hole (Γ–X)	1.47	7.19	232.6	0.044
	Hole (Γ–Y)	1.47	7.19	232.4	0.044

3.4 Photocatalytic properties

Fig. 4a shows the band-gap changes as functions of applied compressive and tensile strains along different directions for h-BCH (left) and t-BCH (right). For h-BCH, the band-gap decreases with compressive strains, while it increases with tensile strains whether under the uniaxial or biaxial stress loading. However, for t-BCH, the band-gap decreases with uniaxial compressive and tensile strains; whereas under the biaxial stress loading, the band-gap decreases with compressive strains and increases with tensile strains. Therefore, the band-gap of strain-modified h-BCH ranges from 2.27 to 1.93 eV using the HSE06 functional, exceeding the free energy of water splitting of 1.23 eV. Such suitable band gaps are located in the visible light region (1.62–3.11 eV), making it an effective 2D material for visible-light-driven overall water splitting. To investigate this possibility, the energy positions of the VBM and CBM for h-BCH were then calculated at the HSE06 level, as shown in Fig. 4b. It can be seen that the VBM and CBM of h-BCH are more positive than the reduction potential of H^+/H_2 and

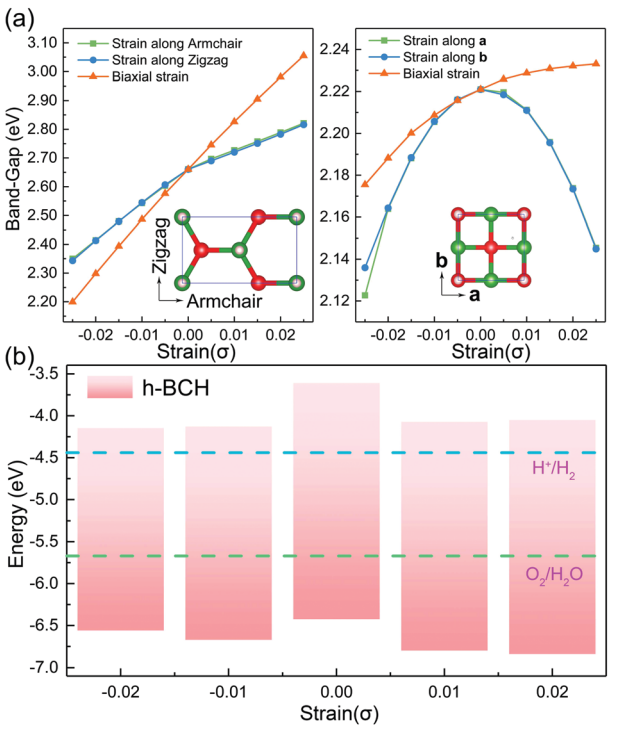

Fig. 4 (a) Electronic band gap of h-BCH (left) and t-BCH (right) cells at various strains calculated using the HSE06 screened hybrid density functional. (b) The calculated band alignment of the h-BCH structure based on the HSE06 screened hybrid density functional. The vacuum level is set to 0 eV. The chemical reaction potentials for H^+/H_2 and O_2/H_2O are also plotted with dashed lines (pH = 0).

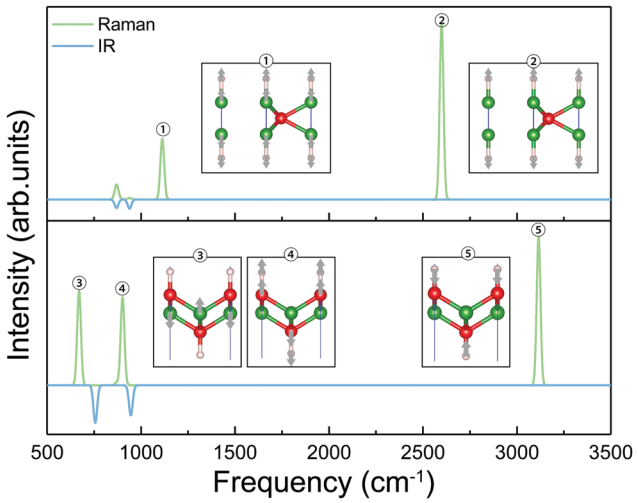

Fig. 5 Theoretically calculated Raman and IR spectra of h-BCH (upper) and t-BCH (lower). The structural motifs are also plotted. Arrows represent the directions of the corresponding oscillation.

more negative than the oxidation potential of O_2/H_2O, respectively, which means that it can be used as a visible-light-driven photocatalyst for hydrogen reduction and oxygen production in overall water splitting. Thus, the calculated band gap and band edge alignment provide persuasive evidence that the h-BCH monolayer is a promising material for overall water splitting.

Additionally, the indirect band gap of h-BCH is certainly a disadvantage for efficient light absorption, but, it does discourage radiative electron–hole pair recombination and might be beneficial for carrier separation.[43] Simultaneously, the most common photocatalyst possesses an indirect band gap.[43,44] On the other hand, the CBM of h-BCH shows a strong isotropic distribution because it mainly consists of symmetrically hybridized B-p and H-s states, forming a well-delocalized wave function (see Fig. 3b). This suggests strongly that the photocatalytic activity of h-BCH does not significantly depend on the orientation, giving a potential high performance photocatalyst for water splitting.

3.5 Raman and IR properties

Raman and IR spectra were simulated based on phonon vibrational modes in the Brillouin zone, which are related to the symmetry of the structure. As shown in Fig. 5, the calculated highest Raman active frequencies are located at 2599 cm^{-1} for h-BCH and 3115 cm^{-1} for t-BCH, respectively. For h-BCH, the out-of-plane vibration of B–H motifs leads to the Raman active mode at 1113 cm^{-1} and the out-of-plane vibration of C–H motifs leads to the Raman active mode at 901 cm^{-1}, respectively. However, the IR spectra of these monolayers exhibit two distinguishing peaks below 1000 cm^{-1}. These Raman or IR spectra would be useful to experimentally check the formation of these 2D structures.

4 Conclusions

In summary, we have theoretically designed two 2D ternary semiconductors, h-BCH and t-BCH, respectively. The state-of-the-art first principles quantum chemical calculations have confirmed the dynamic, thermal, and mechanical stabilities of these new structures, respectively, by their phonon dispersion characteristics, AIMD simulations at 300 K, and mechanical criteria. The calculated band structure and DOS reveal that the proposed monolayers are semiconductors with high electron mobility (7.41×10^3 cm^2 V^{-1} s^{-1}), which is higher than those of some experimental synthetic 2D materials (*i.e.*, ~ 200 cm^2 V^{-1} s^{-1} for MoS_2). Moreover, our theoretical calculations highlight that h-BCH satisfies the requirement for the reduction and oxidation levels for overall visible-light water splitting. All these results demonstrate that the designed 2D BCH material with high mobility can be comparable to other 2D derivatives. Our findings give novel materials that can be applied in future nano-devices and photocatalysts.

Conflicts of interest

There are no conflicts to declare.

Acknowledgements

The work was carried out at the National Supercomputer Center in Guangzhou, and the calculations were performed on TianHe-2. This work was supported by the National Natural Science Foundation of China (Grant No. 11504325, 50972129, and 50602039) and the European Union's Horizon 2020 Research and Innovation Staff Exchange (RISE) Scheme (No. 734578), Natural Science Foundation of Zhejiang Province (LQ15A040004). This work was also supported by the International Science Technology Cooperation Program of China (2014DFR51160), the Key Project of the National Natural Science Foundation of China (U1809210) and the One Belt and One Road International Cooperation Project from the Key Research and Development Program of Zhejiang Province (No. 2018C04021).

References

1 S. Zhang, M. Xie, F. Li, Z. Yan, Y. Li, E. Kan, W. Liu, Z. Chen and H. Zeng, *Angew. Chem.*, 2016, **128**, 1698–1701.
2 T. Yu, S. Zhang, F. Li, Z. Zhao, L. Liu, H. Xu and G. Yang, *J. Mater. Chem. A*, 2017, **5**, 18698–18706.
3 L. Li, Y. Yu, G. J. Ye, Q. Ge, X. Ou, H. Wu, D. Feng, X. H. Chen and Y. Zhang, *Nat. Nanotechnol.*, 2014, **9**, 372.
4 Y. Liang, Y. Dai, Y. Ma, L. Ju, W. Wei and B. Huang, *J. Mater. Chem. A*, 2018, **6**, 2073–2080.
5 Z. Guo, J. Zhou and Z. Sun, *J. Mater. Chem. A*, 2017, **5**, 23530–23535.
6 C. Tan, X. Cao, X.-J. Wu, Q. He, J. Yang, X. Zhang, J. Chen, W. Zhao, S. Han and G.-H. Nam, *et al.*, *Chem. Rev.*, 2017, **117**, 6225–6331.
7 G. R. Bhimanapati, Z. Lin, V. Meunier, Y. Jung, J. Cha, S. Das, D. Xiao, Y. Son, M. S. Strano and V. R. Cooper, *et al.*, *ACS Nano*, 2015, **9**, 11509–11539.
8 P. Miró, M. Audiffred and T. Heine, *Chem. Soc. Rev.*, 2014, **43**, 6537–6554.

9 L. Liao, Y.-C. Lin, M. Bao, R. Cheng, J. Bai, Y. Liu, Y. Qu, K. L. Wang, Y. Huang and X. Duan, *Nature*, 2010, **467**, 305.
10 F. Schwierz, *Nat. Nanotechnol.*, 2010, **5**, 487.
11 H. Liu, A. T. Neal, Z. Zhu, Z. Luo, X. Xu, D. Tománek and P. D. Ye, *ACS Nano*, 2014, **8**, 4033–4041.
12 A. Ziletti, A. Carvalho, D. K. Campbell, D. F. Coker and A. C. Neto, *Phys. Rev. Lett.*, 2015, **114**, 046801.
13 V. Georgakilas, J. N. Tiwari, K. C. Kemp, J. A. Perman, A. B. Bourlinos, K. S. Kim and R. Zboril, *Chem. Rev.*, 2016, **116**, 5464–5519.
14 V. Georgakilas, M. Otyepka, A. B. Bourlinos, V. Chandra, N. Kim, K. C. Kemp, P. Hobza, R. Zboril and K. S. Kim, *Chem. Rev.*, 2012, **112**, 6156–6214.
15 Q. Zhu, Y. Lu and J. Jiang, *J. Phys. Chem. Lett.*, 2011, **2**, 1310–1314.
16 Y. Jiao, F. Ma, J. Bell, A. Bilic and A. Du, *Angew. Chem.*, 2016, **128**, 10448–10451.
17 L. Zhu, S.-S. Wang, S. Guan, Y. Liu, T. Zhang, G. Chen and S. A. Yang, *Nano Lett.*, 2016, **16**, 6548–6554.
18 H. Pan, H. Zhang, Y. Sun, J. Li, Y. Du and N. Tang, *Phys. Rev. B*, 2017, **96**, 195412.
19 J. Mahmood, E. K. Lee, M. Jung, D. Shin, I.-Y. Jeon, S.-M. Jung, H.-J. Choi, J.-M. Seo, S.-Y. Bae and S.-D. Sohn, *et al.*, *Nat. Commun.*, 2015, **6**, 6486.
20 B. Mortazavi, M. Makaremi, M. Shahrokhi, M. Raeisi, C. V. Singh, T. Rabczuk and L. F. C. Pereira, *Nanoscale*, 2018, **10**, 3759–3768.
21 D. Fan, S. Lu, Y. Guo and X. Hu, *J. Mater. Chem. C*, 2018, **6**, 1651–1658.
22 D. Fan, S. Lu, Y. Guo and X. Hu, *J. Mater. Chem. C*, 2017, **5**, 3561–3567.
23 B. Radisavljevic, A. Radenovic, J. Brivio, I. V. Giacometti and A. Kis, *Nat. Nanotechnol.*, 2011, **6**, 147.
24 G. Kresse and J. Furthmüller, *Phys. Rev. B: Condens. Matter Mater. Phys.*, 1996, **54**, 11169.
25 M. Gajdoš, K. Hummer, G. Kresse, J. Furthmüller and F. Bechstedt, *Phys. Rev. B: Condens. Matter Mater. Phys.*, 2006, **73**, 045112.
26 P. E. Blöchl, *Phys. Rev. B: Condens. Matter Mater. Phys.*, 1994, **50**, 17953.
27 J. Heyd, G. E. Scuseria and M. Ernzerhof, *J. Chem. Phys.*, 2003, **118**, 8207–8215.
28 A. Togo and I. Tanaka, *Scr. Mater.*, 2015, **108**, 1–5.
29 S. Grimme, *J. Comput. Chem.*, 2006, **27**, 1787–1799.
30 A. Fleurence, R. Friedlein, T. Ozaki, H. Kawai, Y. Wang and Y. Yamada-Takamura, *Phys. Rev. Lett.*, 2012, **108**, 245501.
31 Y. Wang, F. Li, Y. Li and Z. Chen, *Nat. Commun.*, 2016, **7**, 11488.
32 Q. Peng, R. Xiong, B. Sa, J. Zhou, C. Wen, B. Wu, M. Anpo and Z. Sun, *Catal. Sci. Technol.*, 2017, **7**, 2744–2752.
33 Q. Wei and X. Peng, *Appl. Phys. Lett.*, 2014, **104**, 251915.
34 C. Lee, X. Wei, J. W. Kysar and J. Hone, *Science*, 2008, **321**, 385–388.
35 Q. Peng and S. De, *Phys. Chem. Chem. Phys.*, 2013, **15**, 19427–19437.
36 D. Fan, S. Lu, Y. Guo and X. Hu, *J. Phys. Chem. C*, 2018, **122**, 15118–15124.
37 S. Bruzzone and G. Fiori, *Appl. Phys. Lett.*, 2011, **99**, 222108.
38 J. Qiao, X. Kong, Z.-X. Hu, F. Yang and W. Ji, *Nat. Commun.*, 2014, **5**, 4475.
39 Q. Wu, W. W. Xu, B. Qu, L. Ma, X. Niu, J. Wang and X. C. Zeng, *Mater. Horiz.*, 2017, **4**, 1085–1091.
40 Z. Zhuo, X. Wu and J. Yang, *J. Am. Chem. Soc.*, 2016, **138**, 7091–7098.
41 Y. Ma, A. Kuc and T. Heine, *J. Am. Chem. Soc.*, 2017, **139**, 11694–11697.
42 Z. Zhu, X. Cai, S. Yi, J. Chen, Y. Dai, C. Niu, Z. Guo, M. Xie, F. Liu and J.-H. Cho, *et al.*, *Phys. Rev. Lett.*, 2017, **119**, 106101.
43 N. Umezawa, O. Shuxin and J. Ye, *Phys. Rev. B: Condens. Matter Mater. Phys.*, 2011, **83**, 035202.
44 S. Ouyang, N. Kikugawa, D. Chen, Z. Zou and J. Ye, *J. Phys. Chem. C*, 2009, **113**, 1560–1566.